SAND2015-3389J

Forest Height, Temperature and Magnetic Field Dependence of the Microwave AC Conductance of Aligned Multiwall Carbon Nanotube Sheets

Brian L. Brown,[1] Patricia Martinez,[1,2] Anvar A. Zakhidov,[1,2]

Eric A. Shaner,[3] and Mark Lee[1]

[1]*Department of Physics, The University of Texas at Dallas, Richardson, TX 75080*

[2]*The Alan G. McDiarmid NanoTech Institute, The University of Texas at Dallas, Richardson, TX 75080*

[3]*Sandia National Laboratories, Albuquerque, NM 87123*

Abstract:

Understanding the performance of multi-walled carbon nanotube (MWNT) sheets in the microwave regime is essential for their potential use in high-speed, high-frequency applications. To expand current knowledge, complex AC conductance measurements from 0.01 to 50 GHz and across temperatures of 4.2 to 300K and magnetic fields up to 2 T were made on sheets of highly aligned MWNTs with strands oriented both parallel and perpendicular to the microwave electric field polarization. Sheets were drawn from 329 and 520 μm-high MWNT forests. Under all conditions, AC conductance is modeled approximately by a shunt capacitance in parallel with a frequency-independent conductance, but with no inductive contribution. This is consistent with diffusive Drude conduction as the primary AC transport mechanism up to 50

GHz. Further, it is found that the AC conductance is essentially independent of temperature and magnetic field.

1. Introduction

Carbon nanotubes (CNTs) have been the subject of widespread study for nearly a quarter century[1], with investigations of single-wall and multi-walled nanotubes (SWNTs, MWNTs) bringing a variety of scientifically interesting and potentially useful properties to light. Going beyond the study of individual nanotubes, significant efforts have been made to use CNTs as the basis of more complex macroscopic structures. In particular, the assembly of nanotubes into multifunctional textile sheets[2,3] has been found to have numerous possible applications. Taking advantage of not only their high electrical conductivity,[2,3] researchers have leveraged the high strength and flexibility of MWNT sheets to develop a counter electrode for dye-sensitized solar cells[4]. In other areas, thermal properties like high steady-state temperature and rapid thermal response time have been enhanced for the use of MWNT sheets as conductive heaters[5], while the transparency and demonstrated DC resistance anisotropy of MWNT sheets suggests they can be used as wire grid polarizers in infrared optics[2].

Including the above examples, most research to date has focused on the mechanical and/or DC electrical properties of MWNT sheets, but an understanding of their AC response is critical to fully utilize these materials in high-frequency, high-speed electronic applications. AC conductance measurements on CNT networks comprised of SWNTs in the GHz range has in many cases[6,7,8,9,10] shown microwave conductance to be dominated by glassy universal disorder dynamics[11]. With specific regard to MWNT textile sheets, we previously reported room-temperature microwave conductance measurements on a set of highly aligned MWNT sheets

drawn from a substrate on which was grown a high density array of vertically-aligned, bamboo-like MWNTs, i.e. a "forest", with a mean height of 420 μm[12]. Results from Ref. 12 stood in contrast to the SWNT–based studies, in that the major features of the MWNT sheets' complex conductance could be approximately modeled by a frequency-independent resistor and capacitor consistent with low-frequency diffusive AC conduction,[13] rather than by glassy dynamics.

In this paper we report on new measurements and modeling of the complex conductance of highly aligned MWNT sheets drawn from different forest heights of 329 and 520 μm. Like the previous sheet studied[12], the alignment of the MWNT strands means that the sheet resistance of these textiles is greater for current flow perpendicular to strand alignment vs. current flow parallel to the alignment. Regarding the forest height of the new sheets, those drawn from the 329 μm forest are characterized as having a higher DC sheet resistance than those drawn from the 520 μm forest for current flow perpendicular to strand alignment, and lower DC sheet resistance for current flow parallel to strand alignment. Therefore, it is of interest to test whether the same trend holds at microwave frequencies. Moreover, the above DC resistance characteristics imply that the DC resistance anisotropy ratio for MWNTs extracted from the shorter forest is greater than that of the taller forest, and we seek to determine whether or not the same correlation exists for the AC conductance anisotropy ratio. In addition, we have examined the frequency dependence of the different MWNT sheets to establish whether similar AC response characteristics exist between forest heights. In all cases, new results are compared to the results of Ref. 12 taken with MWNT sheets drawn from a forest height of 420 μm.

Measurements were taken across a frequency band of 0.01 to 50 GHz, and temperatures, 4.2 K to 300 K, with the MWNT strands oriented either parallel or perpendicular to the microwave electric field polarization. Additionally, AC conductance measurements in magnetic fields up to

2 T were taken at 4.2 K. In all cases, the complex microwave conductance can be approximately modeled with a simple circuit consistent with previous results. Further, it is found that the AC conductance anisotropy ratio is greater for the shorter forest, consistent with measurements taken for the DC resistance anisotropy, and that the AC conductance is essentially independent of temperature and magnetic field.

This paper is organized as follows. Section 2 describes fabrication and DC electrical characterization of MWNT sheets measured. Section 3 outlines the equipment and experimental procedures. Section 4 presents the raw data obtained in the form of *S*-parameters as a function of frequency. Section 5 details the extraction of AC conductance from the *S*-parameter data and develops a representative circuit model. Section 6 analyzes data in the context of the circuit model. Section 7 presents and discusses AC conductance data as a function of temperature and magnetic field. Section 8 summarizes our conclusions.

2. Sample Fabrication and Characterization

MWNT forests were grown by catalytic chemical vapor deposition (CVD) on a <100> silicon substrate bearing 50 nm of thermal oxide and seeded with a 3 nm iron catalyst film deposited by electron-beam evaporation. The MWNT forests grew from a gas mixture of He/H_2 (56%) and He/C_2H_2 (5%) with a 3865 sccm flow rate inside of a quartz reactor maintained at a pressure 1 atm. One forest was grown at a temperature of 730 ^oC for 10 minutes, resulting in a mean forest height of 329 μm with areal mass density of 4.2 $\mu g/cm^2$ (Fig. 1(a)). A second forest was grown at a temperature of 750 ^oC for 10 minutes, resulting in a mean forest height of 520 μm with areal mass density of 2.5 $\mu g/cm^2$. Self-supporting, highly aligned MWNT sheets were dry-drawn from the sidewalls of each forest in a manner described in detail in Ref. 2. Areal

densities for the free-standing sheets after being drawn were 6.4 μg/cm^2 for the 329 μm forest sheet and 7.9 μg/cm^2 for the 520 μm forest sheet.

Segments measuring ~ 1cm long by 0.5 cm wide were cut from each drawn sheet in order to cover fully the ground-signal-ground (*g*-*s*-*g*) gaps of microwave co-planar waveguides (CPWs). Each MWNT sheet was assembled onto a CPW and adhered by wetting with drops of isopropanol and subsequent alcohol evaporation. During this procedure, surface tension in the sheets was reduced, resulting in the densification of the MWNT sheet for better adherence to the substrate. Scanning electron microscope images show densified sheets to be composed of an entangled network of long, highly aligned MWNT strands extended with a dominant directional alignment (Fig. 1(b)). For the device assembled with MWNTs from the 329 μm-high forest, two-point DC measurements using silver print contacts gave sheet resistances (including contact resistance) of 7700 ± 1284 Ω/□ for current perpendicular (⊥) to the strand alignment and 340 $\pm$ 20 Ω/□ for current parallel (□) to the alignment for an anisotropy ratio of $R(\perp)/R(\square) = 22.6 \pm 5.5$. Sheet resistances for the device assembled using MWNTs from the 520 μm-high forest were 4780 ± 1494 Ω/□ for perpendicular (⊥) alignment and 353 ± 19 Ω/□ for parallel (□) alignment for an anisotropy ratio of $R(\perp)/R(\square) = 13.5 \pm 5.0$.

Construction and characterization of the bare CPWs is described in detail in Ref.6 and summarized here. All CPWs consisted of three gold (Au) thin films lithographically patterned into a ground-signal-ground configuration (*g*-*s*-*g*) on a fused quartz susbstrate using a layer of titanium (Ti) to aid in adhesion. Each CPW was covered by a 100 nm insulating layer of Si_3N_4. Thus, the MWNT sheets assembled on top of the CPWs coupled capacitively to the microwave field so that contact resistance effects were avoided. MWNTs sheets drawn from the 329 μm-high forest and the 520 μm-high forest were then assembled onto CPW substrates in the manner

described in the previous paragraph. For each forest height two samples were measured: dominant MWNT strand orientation aligned (1) parallel $(\square)$ and (2) perpendicular $(\perp)$ to the polarization of the microwave electric field in the signal-to-ground gaps of the CPW (Fig. 2(a) and Fig 2(b)).

3. Experimental Technique and Protocol

Phase-sensitive microwave reflection and transmission measurements were made using a two-port vector network analyzer (VNA) (Agilent N5245A). VNA signals were coupled to/from a CPW using a pair of 150 um pitch *g*-*s*-*g* probes (GGB 67A-GSG-150) touched down at either end of the CPW. The system was calibrated across the 0.01-to-50 GHz band to 50 ohm characteristic impedance up to the plane of the probe tips using a commercial short-open-load-thru (SOLT) calibration substrate (GGB CS-5). All data presented were taken with samples in vacuum to prevent air or moisture absorption.

Magnitudes and phases of the voltage scattering parameters or *S*-parameters $S_{ij}(i, j = 1, 2)$ were measured as a function of frequency, *f*. CPWs with and without assembled MWNT sheets were symmetric with respect to the waveguide ports (indexed 1 and 2) at either end of the CPWs, so the reflection parameter (return loss) $S_{11} = S_{22}$ and transmission parameter (insertion loss) $S_{21} = S_{12}$ to within experimental accuracy. Experimental procedure was as follows: *S*-parameters were first measured for "bare" CPWs, i.e., CPWs with no MWNT sheet. The *S*-parameters of all bare CPWs were the same to within 5% variance. MWNT sheets were then assembled on designated CPWs and the *S*-parameters of these "assembled" CPWs, i.e. CPWs with MWNT sheets, were re-measured. One CPW was left bare as a control to monitor systematic repeatability of measurements taken prior to and after MWNT sheet assembly. Post-assembly

measurements showed that the control CPW's *S*-parameters matched those of the original bare CPWs to within the nominal 5% variance.

Temperature was monitored and controlled using a cryogenic temperature controller (Lakeshore Model 336). The probe station sample stage was cooled with liquid He to an initial temperature of 4.2 K, then heated in order to record measurements at various temperature setpoints up to room temperature. The *g-s-g* probes were lifted during temperature transitions to avoid damage to the CPW electrodes caused by possible shifts in probe position due to differential thermal expansions. Probes were set down on the CPW once the temperature stabilized at each setpoint to within ±2% variance, and the system was re-calibrated to 50 ohms characteristic impedance. SOLT structures on the calibration substrate showed less than 1% variance over the full temperature range, implying there should be little to no loss of measurement accuracy at low temperatures. Once a measurement was recorded, the probes were lifted again in preparation for the transition to the next temperature value.

At the base temperature of 4.2 K, a magnetic field was applied normal to the plane of the CPWs using a vertical superconducting magnet and power supply (Lakeshore Model 625). The *g-s-g* probes were then landed on the CPW ends and *S*-parameter measurements were taken over a range of field strengths from 0 to 2.0 T. This was done at a constant temperature of 4.2 K, allowing the probes to remain in place and not be lifted during magnetic field transitions.

4. S-parameter Data

The magnitudes and phases of the measured reflection S_{11} and transmission S_{21} amplitudes are shown in Figs. 3-5. In Figs. 3(a-b), magnitude data for bare/control CPWs without MWNT sheets are displayed using black curves, while data from assembled CPWs with MWNT sheets

are displayed with alternate colors. The *S*-parameter magnitude data shown for assembled CPWs are not de-embedded from bare CPW *S*-parameters.

S-parameter phase characteristics were quantitatively similar among all bare CPWs and qualitatively similar among all assembled CPWs, so typical results from one bare and one assembled CPW are shown in Figs. 4 and 5. Phase data for S_{11} of a bare CPW is displayed in black, while that of a CPW assembled with MWNT sheets is displayed in red in Fig. 4. S_{21} phase data for bare CPWs is shown in Fig. 5(a) and for a CPW assembled with MWNT sheets in Fig 5(b). The phase data for assembled CPWs in Figs. 4 and 5(b) have been de-embedded from the raw phase measurements in order clearly isolate phase changes due only to the placement of the sheets.

All bare CPWs were well-matched to the 50 Ω system based on the reasonably small values of $|S_{11}|$ obtained on the bare waveguides, as seen in the black curve of Fig. 3(a). $|S_{11}|$ was measured at < -10 dB across the full frequency range and ≤ -20 dB at all frequencies above 7 GHz, giving a voltage standing wave ratio of $\mathrm{VSWR} \leq 1.22$ and a bare CPW characteristic impedance of $40\,\Omega \leq Z_o \leq 60\,\Omega$. The assembly of MWNT sheets across the *g*-*s*-*g* gaps of the CPWs caused a significant impedance mismatch when placed in either a parallel or perpendicular orientation, resulting in obvious changes in $|S_{11}|$, which increased to between -2 and -10 dB across the full measurement band (remaining curves, Fig. 3(a)).

Additional insertion loss also resulted from the MWNT sheet assembly, as demonstrated by the far greater insertion loss in $|S_{21}|$ when comparing bare/control CPWs to those with the MWNT sheets (black curve represents bare/control, Fig. 3(b)). $|S_{21}|$ for all bare/control CPWs was measured at > –10 dB prior to assembly. After assembly of any MWNT sheet on a CPW, $|S_{21}|$ was reduced to between -10 and -70 dB across the measurement band. While some of this

reduction may be attributed to resistive absorption in the MWNT sheet, most is due to the sheet shunting AC current to ground prior to reaching the termination port. Evidence of this can be seen in the magnitude and phase of the reflection S_{11} for CPWs assembled with MWNT sheets, since a phase near 180^{o} (red curve, Fig. 4) and magnitude near 0 dB (Fig. 3(a)) imply that the presence of the assemble sheet approximates a short circuit.

Comparing S_{21} phase characteristics, Fig. 5(b) indicates that placement of a MWNT sheet also reduces the phase velocity v_p of the propagating signal, since the frequency interval $\Delta f \propto v_p$ decreases compared to that of the bare CPW in Fig. 5(a). Data also show that phase velocities differ between orientations, with MWNT sheets drawn from the 329 um forest being slower in parallel orientation, and MWNT sheets drawn from the 520 um forest being slower in perpendicular orientation. Analysis of the data taken for MWNT sheets drawn from the 420 um forest in our earlier study showed them to be slower in parallel orientation as well. Reduced phase velocities also mean that the refraction index $n = c / v_p$ of the assembled CPWs increases relative to the bare CPW. Computations for bare CPWs (including the silicon nitride layer) resulted in a refractive index of $n(\text{bare}) \approx 1.5,$ while the relative refractive index for CPWs assembled with MWNT sheets ranged from $n(\text{assembled}) \approx 2.9$ to 8.2.

5. Complex AC Conductance and Circuit Model

The high conductivity of Au and the low loss tangents for fused quartz and silicon nitride ($\square\ 10^{-4}$) allow the bare CPWs to be accurately modeled as a standard lossy transmission line[14] with series (signal in to signal out) resistance R and inductance L per unit length of transmission line and shunt (signal to ground) conductance per unit length due solely to the capacitance between signal and ground conductors. A standard analysis[14] of the bare/control CPW *S*-

parameters yields a bare series inductance of $L_{bare} = 2.2 \pm 0.05$ nH/cm and a bare shunt capacitance of $C_{bare} = 1.2 \pm 0.05$ pF/cm, including the Si_3N_4. The frequency dependence of the bare $|S_{21}|$ data (Fig. 3(b)) indicates that the series resistance $R_{bare}(\omega) \propto -\log |S_{21}|$ is well modeled by the $f^{1/2}$ frequency dependence characteristic of series surface resistance loss in the Au electrodes[14].

The assembly of the MWNT sheets across the *g*-*s*-*g* gaps of a previously bare CPW is electrically modeled by adding an additional AC shunt path connected to the transmission line with a shunt conductance *Y* that may not be simply capacitive (Fig. 6(a)). Determination of the shunt conductance *Y* for each assembled CPW begins with the standard de-embedding procedure detailed in Ref. **15**. The raw *S*-parameter data are a measurement of the total AC conductance including contributions from the device under test (DUT), i.e. the section of an assembled CPW covered by a MWNT sheet, cascaded with segments of the CPW on either side of the DUT that remain bare. De-embedding the DUT isolates out its *S*-parameters from the raw measured data. This allows *Y* to be extracted by exploiting differences in the propagation constant and characteristic impedance of the assembled vs. bare CPWs.

The resulting real and imaginary components of *Y* are plotted using red curves in Fig. 7(a) and 7(b) for parallel and perpendicular orientations, respectively, on devices with MWNT sheets drawn from the 329 μm-high forest, and in Fig. 7(c) and 7(d) for parallel and perpendicular orientations, respectively, on devices with sheets drawn from the 520 μm-high forest. In each of the four combinations of orientation and forest height, Re(*Y*) shows low a distinct frequency roll-off and relatively weak frequency dependence at high frequencies, while Im(*Y*) is reasonably approximated to first order by a linear frequency dependence.

The gross shape of the frequency dependence of $Y(f)$ extracted from devices assembled with sheets drawn from 329 and 520 μm-high forests can be described by the simple circuit shown in Fig. 6(b). Physically, the Au signal electrode couples capacitively to the MWNT sheet, represented by the conductance G_{sheet}, which in turn couples capacitively to the Au ground plane. For simplicity, the impedances of the two series contact capacitive components are combined and represented by an equivalent $C_{contact}$. In parallel, the shunt capacitance C_{shunt} effectively replaces C_{bare} from the transmission line model, since the MWNT sheet fills the near surface *g*-*s*-*g* volumes that were occupied by vacuum on the bare CPW. This is the same circuit used to model the AC conductance behavior of 420 μm-high forests we reported previously[12]. Electrically, $C_{contact}$ models the low frequency roll-off in Re(Y), which is directly attributable to the capacitive contact between the MWNT sheets and the Au electrodes, while G_{sheet} models the weak frequency dependence at high frequencies. The first order linear behavior at high frequency seen in extracted Im(Y) is modeled by C_{shunt} in parallel. This circuit effectively models the AC conductance on devices with MWNTs in either a parallel (□) or perpendicular (⊥) orientation, as is illustrated using blue curves in Fig. 7(a-d).

Circuit parameters calculated to construct the model for each Re(Y) and Im(Y) are summarized in Table 1 (values from our previous study of a 420 μm-high forest are included for comparison). The AC conductance curves in Fig. 7(a-d) show that these parameters are not an optimized fit, since one set of values is used to describe both Re(Y) and Im(Y). They should be viewed as coarse values intended only to capture the major frequency trends of the complex conductance introduced by the assembly of MWNT sheets onto the CPWs. It is also clear that the extracted $Y(f)$ data shows finer frequency dependent details that cannot be properly represented by any simple circuit model.

6. Data Analysis

Referencing Table 1, extracted circuit model values are physically reasonable for both the present work and previously reported results. Each assembled MWNT sheet has a contact capacitance on the order of 10 to 100 pF/cm, which is in the range of values obtained when calculating the capacitance classically based on the physical geometry. Estimates are obtained by multiplying the capacitance of a single MWNT (i.e. a wire) separated from a conducting plane[16] by 100 nm of Si_3N_4 by the number of MWNTs covering the CPW based on the average placement density.

Regarding AC performance, the MWNT sheet conductance for textiles drawn from both the 329 μm and 520 μm-high forests presented here is consistent with low-frequency diffusive (Drude) AC conduction $\sigma(f)$,[13] since in the low frequency limit $\mathrm{Re}\,\sigma \approx \text{constant}$ after subtracting the effects of contact capacitance and $\mathrm{Im}\,\sigma \propto f$. Moreover, at high frequencies, there is no evidence of an inductive contribution which would cause $\mathrm{Re}\,\sigma$ and $\mathrm{Im}\,\sigma$ to roll off, which implies the AC dynamics of the MWNT sheets is dominated by diffusive scattering up to 50 GHz. This is consistent with the AC conduction behavior found for the 420 μm-high forest from our prior study[12]. Further comparing to the literature, diffusive conduction has been previously reported for single MWNTs,[17] as well as for SWNT "mats"[18], while the conduction method for several other SWNT formats[6,7,8,9,10] has been interpreted as having "universal disorder" or glass-like AC response[11].

Relating AC conduction results to the different MWNT forest heights examined, we find that the frequency response characteristics are similar for both the 329 μm and 520 μm-high forests presented here, as well as for the 420 μm-high forest from our prior study. This applies to

MWNT sheets assembled in either the parallel or perpendicular orientation. Further comparing conductance results between forest heights (including those from the 420 μm-high forest we previously reported), we find that sheets drawn from the 329 μm-high forests have a higher conductance in both orientations. While this is consistent with the shorter forest having smaller sheet resistance in parallel orientation, it reverses the trend that the shorter forest has higher DC resistance in the perpendicular orientation. For the sheet conductance anisotropy ratios, $G_{sheet}(\square) / G_{sheet}(\perp)$, comparing the 329 and 520 μm-high forests we find a correlation with DC resistance anisotropy ratio in being greater for the short forest as seen in Table 2. However, the 420 μm-high forest from our previous study does not fit the pattern since its conductance anisotropy ratio is the largest the three. The absence of a consistent trend between the three forests for extracted conductivity in Table 1 and the associated anisotropy ratios in Table 2 could simply be a function of the uncertainty in 2-pt DC resistance measurements quoted in Section 2. Variation may also be introduced through differing growth conditions between MWNT sheets, methods of probing and/or the influence of contacts, or differences in the amount of CPW adherence achieved with sheet densification.

The relative permittivity for the MWNT sheets can be estimated using the refractive indexes calculated for bare and assembled CPWs, based on $\varepsilon_r = n^2$. Prior to assembling a MWNT sheet, a portion of the field propagates in the bare CPW (consisting of the quartz substrate and silicon nitride layer) with the remaining field propagating in vacuum. Assuming the MWNT sheet fills the volume near the *g*-*s*-*g* gaps of the CPW previously filled by vacuum, the relative permittivity for the bare CPW, $\varepsilon_r(\text{bare}) = 2.25$, can be subtracted from the values found for assembled CPWs, $\varepsilon_r(\text{assembled}) \approx 8.2 \text{ to } 66.6$, to arrive at a refractive index for the MWNT sheets. From the values given, a range of relative permittivity values for the MWNT sheets is

found to be $\varepsilon_r(\text{MWNT}) \approx 5.9$ to 64.4. This is a wider range of values compared to existing work, where relative permittivity values between $\text{Re}(\varepsilon_r) \approx 5$ and 20 (from 20 to 50 GHz) have been reported for various SWNT/MWNT mixtures.[19]

7. Temperature and Magnetic Field Effects

Plots of Re(Y) as a function of temperature and magnetic field are illustrated in Fig. 8(a) and Fig. 8(b), respectively, for CPWs assembled with MWNT sheets drawn from the 329 and 520 μm-high forests, and placed in the perpendicular (⊥) orientation. Data is shown at the midband frequency of 25 GHz, with similar trends being observed at other points along the measurement band. Values of Re(Y) were the same within 10% variance across temperatures from 4 to 300 K (Fig. 8(a)) and magnetic fields up to 2 T (Fig. 8(b)), indicating these factors had no discernible effect on conductance across the full frequency range.

The essentially temperature independent AC conductance for MWNT sheets shown here are likely a reflection of the dominance of defect and impurity scattering in these materials. It is expected that MWNT sheets will have higher levels of defect scattering due to entanglement (kinks and intersections) between strands, something which is not present in short, individual MWNTs. Mechanisms related to defect and impurity scattering occur independent of temperature, however, leaving only inelastic scattering in the form of lattice vibrations (phonons) to consider. For these modes, even at room temperature, contributions from both acoustic and optical modes are negligible compared to static scattering events like those associated with impurities or entanglement. This is because acoustic phonons couple very weakly to electrons in graphene[20,21,22] with scattering rates on the order of 10^{11} s^{-1}, and the energies of optical phonons are too high ($\hbar\Omega > 150$ meV) for them to be a factor[23] at temperatures ≤ 300 K.

Absence of magnetic field variation in the AC conductance for MWNT sheets may be attributed in part to the quasi-one-dimensional structure of the underlying nanotubes and the confinement of electron transport along a single axis. This makes it more difficult for electrons in motion to be deflected into a circular trajectory under the influence of a magnetic field perpendicular to their velocity[13].

Comparing to existing work, a lack of significant temperature dependence has been shown for other MWNT sheets at higher temperatures[24,25] and after the removal of amorphous carbon contamination[26]. This is in contrast to the greater temperature dependence seen in SWNT ropes[27] and an isotropic SWNT sheet,[2] as well as in individual MWNTs[28] (down to below 1K), DWNT/MWNT composites[29] (down to 77 K), and MWNT sheets and yarns[30] (down to 3 K) at lower temperatures. Synthesis methods and sample pretreatment affecting the properties of CNTs are one possible source of changes in resistivity, and by extension the conductivity of different CNT assemblies as discussed in Ref. **31**. These results showed densified MWNT sheets and MWNT bucky-papers had weaker temperature dependence than 3-layer MWNT sheets, one-ply and three-ply yarns. Finally, the individual MWNTs in Ref. **28** also differed from our results in that they were shown to have magnetic field dependencies upwards of 14 T, though the transport mechanism was characterized as being due to effects occurring in disordered conductors of reduced dimension, rather than a Drude-like mechanism.

8. Conclusions

In summary, we have measured the real and imaginary AC conductance of MWNT sheets drawn from 329 and 520 μm-high forests with strands oriented both parallel and perpendicular to the microwave electric field polarization. Consistent with our prior work on MWNT sheets

drawn from a 420 μm-high forest, AC conduction mechanisms in the materials examined are diffusive up to 50 GHz and can be described by a simple circuit consisting of a shunt capacitance in parallel with a frequency-independent conductance. The influence of MWNT forest height was examined in relation to the conductivity anisotropy ratio, which was larger for the 329 μm-high forest compared to the 520 μm-high forest and is consistent with the associated DC anisotropy ratio. However, the previously reported conductivity anisotropy ratio for a 420 μm-high forest is greater than both, suggesting conductivity trends may be limited to to within experimental lots prepared under similar conditions. Finally, for all samples examined, AC conduction was essentially independent of temperature (4.2 K $\leq T \leq$ 300 K) and magnetic field (up to 2 T).

Acknowledgments: Work at Sandia and UTD Department of Physics was supported by the DOE Office of Basic Energy Sciences. Sandia National Laboratories is a multi-program laboratory managed and operated by Sandia Corporation, a wholly owned subsidiary of Lockheed Martin Corporation, for the U.S. Department of Energy's National Nuclear Security Administration under contract DE-AC04-94AL85000. Work at the UTD McDiarmid NanoTech Institute was supported by the US Air Force Office of Scientific Research (via contract FA9550-09-1-0384 on "Strengthening Superconductivity in Nanostructures").

Tables

Table 1

Circuit Model Parameters

Forest Height	Orientation	Sheet Resistance ($\Omega/\square$)	G_{sheet} (Ω^{-1}/cm)	C_{shunt} (pF/cm)	$C_{contact}$ (pF/cm)
329 μm	(∥)	340 ± 20	4.3	6.8	33
	(⊥)	7700 ± 1284	1.1	5.8	12
420 μm	(∥)	540 ± 46	2.2	18	40
	(⊥)	7100 ± 1120	0.35	5.6	10
520 μm	(∥)	353 ± 19	1.7	21	30
	(⊥)	4780 ± 1494	0.75	5	10

Table 2

DC Resistance and AC Conductance Anisotropy Ratios

Forest Height	$R(\perp) / R(\parallel)$	$G_{sheet}(\parallel) / G_{sheet}(\perp)$
329 μm	22.6	3.9
420 μm	13	6.3
520 μm	13.5	2.3

Figure Captions

Fig. 1. (a) Scanning electron microscope image of a 329 μm-high forest of multi-walled carbon nanotubes. (b) Scanning electron microscope image of a section of a MWNT sheet drawn from a 329 μm-high forest showing bundles, fibrils and forks.

Fig. 2. (a) Optical microscope image of a MWNT sheet assembled over the Au ground-signal-ground (*g*-*s*-*g*) conductors of a CPW, with the MWNT strands aligned parallel to the electric field (*E*) polarization across the gaps (indicated by the red arrow). The *g*-*s*-*g* gaps are both 3μm wide. (b) Optical microscope image of a MWNT sheet assembled over the *g*-*s*-*g* conductors of a CPW, with the MWNT strands aligned perpendicular to the electric field (*E*) polarization.

Fig. 3. (a) Measured reflection $|S_{11}|$ (dB) and (b) transmission $|S_{21}|$ (dB) amplitudes for bare CPWs (black curves) and those assembled with MWNT sheets (remaining colors). The *S*-parameter data shown for assembled CPWs are not de-embedded from bare CPW *S*-paramters.

Fig. 4. Measured phase of the reflection S_{11} for a bare CPW (black curve) and a CPW assembled with a MWNT sheet (red curve). Phase data for the assembled CPW have been de-embedded from the raw phase measurements.

Fig. 5. (a) Measured phase of the transmission S_{21} for (a) a bare CPW (i.e. without MWNT sheet). (b) De-embedded phase of the transmission S_{21} for a CPW assembled with MWNT sheet. Phase data for the assembled CPW have been de-embedded from the raw phase measurements.

Fig. 6 (a) Transmission line model with generalized Y due to MWNT sheet. (b) Circuit model for generalized Y depicted in Fig. 6(a).

Fig. 7. Shunt conductance Y per unit length for MWNT sheets from data (red curves) and computed from a circuit model (blue curves). Top: Re (Y) and Im(Y) (left-to-right) for a MWNT sheet drawn from a 329 μm-high forest aligned (a) parallel and (b) perpendicular to the electric field polarization. Bottom: Re (Y) and Im(Y) (left-to-right) for a MWNT drawn from 520 μm-high forest aligned (c) parallel and (d) perpendicular to the electric field polarization. Insets: Illustration of a MWNT assembled on a CPW with strands oriented parallel (a,c) and perpendicular (b,d) to the electric field ($\boldsymbol{E}$) polarization near the gaps.

Fig. 8. Measured Re (Y) at 25 GHz for MWNT sheets taken from a 329 μm-high forest (solid blue lines) and a 520 μm-high forest (dashed red lines curves) as a function of (a) temperature and (b) magnetic field. Data taken for MWNT sheets placed in the perpendicular ($\perp$) orientation.

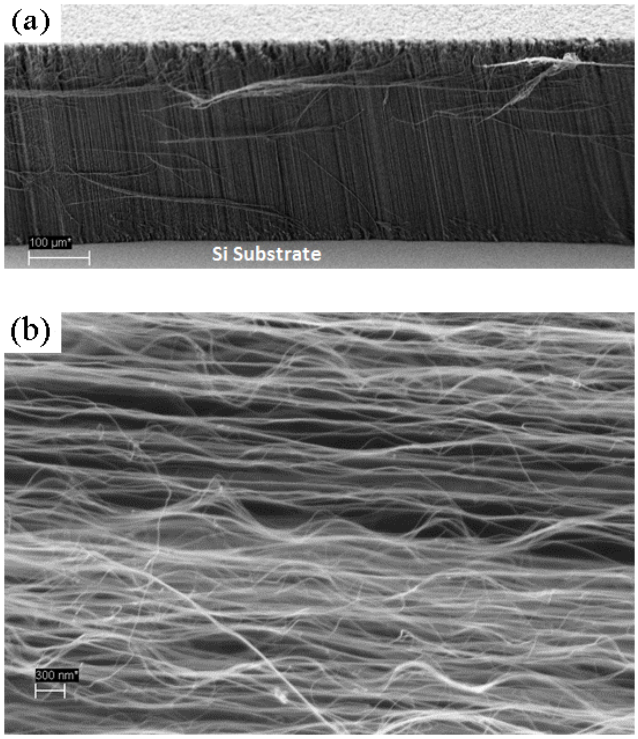

Figure 1

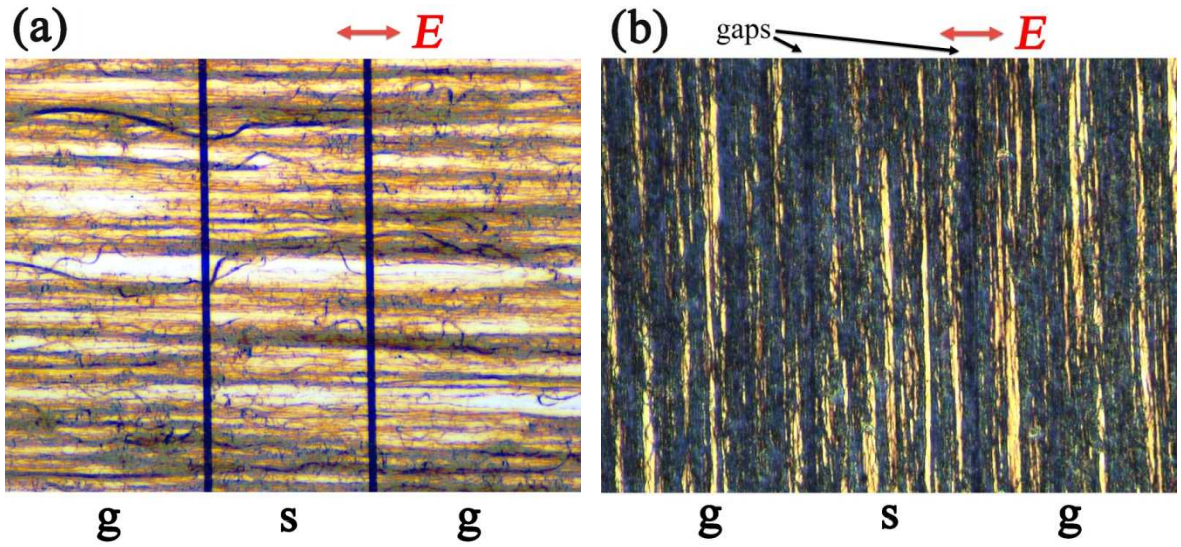

Figure 2

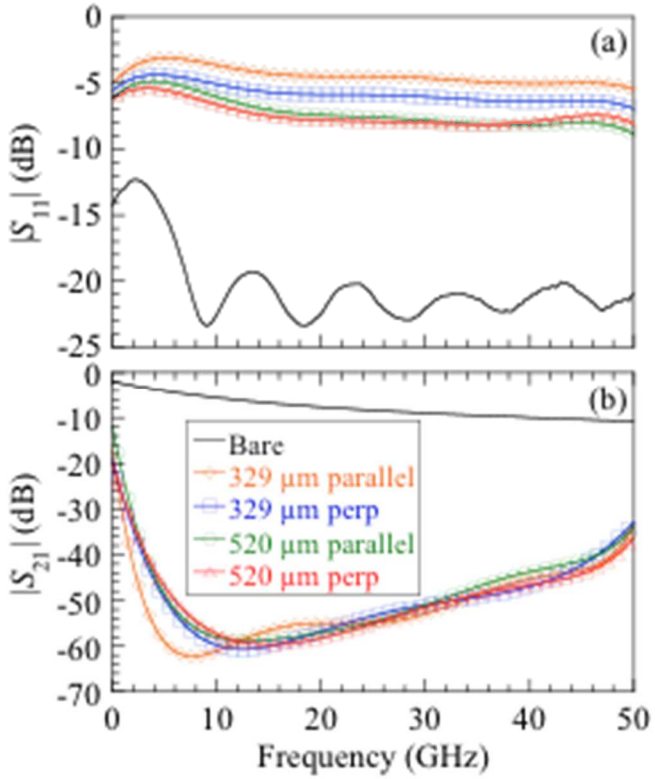
(a)
(b)
$|S_{11}|$ (dB)
$|S_{21}|$ (dB)
Bare
329 µm parallel
329 µm perp
520 µm parallel
520 µm perp
Frequency (GHz)

Figure 3

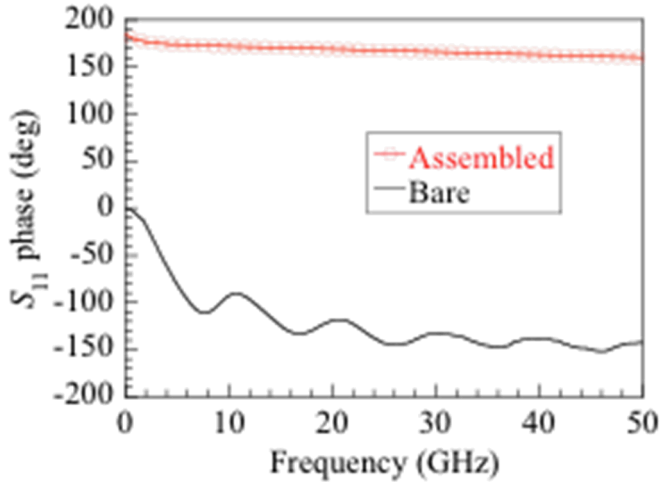
200
150
100
50
0
-50
-100
-150
-200
S_{11} phase (deg)
0
10
20
30
40
50
Frequency (GHz)
Assembled
Bare

Figure 4

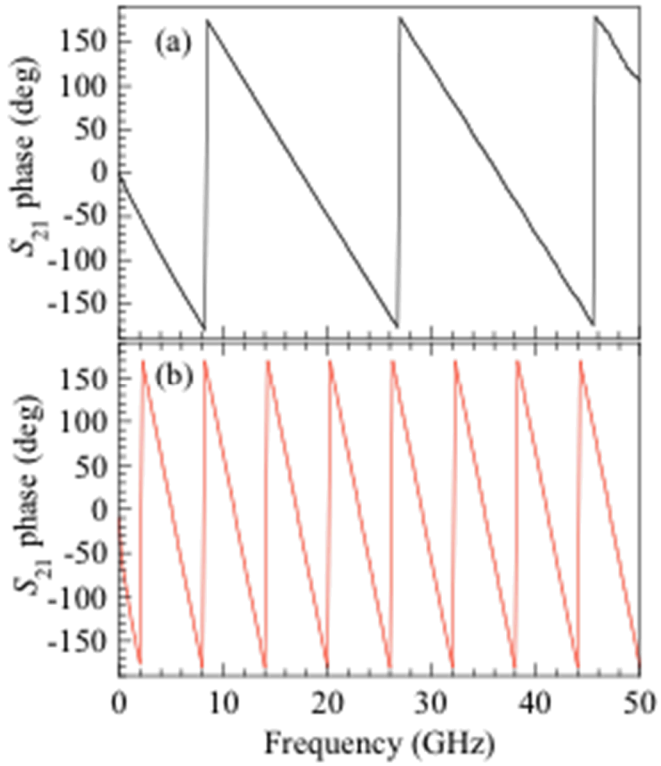
(a)
(b)
S_{21} phase (deg)
150
100
50
0
-50
-100
-150
0
10
20
30
40
50
Frequency (GHz)

Figure 5

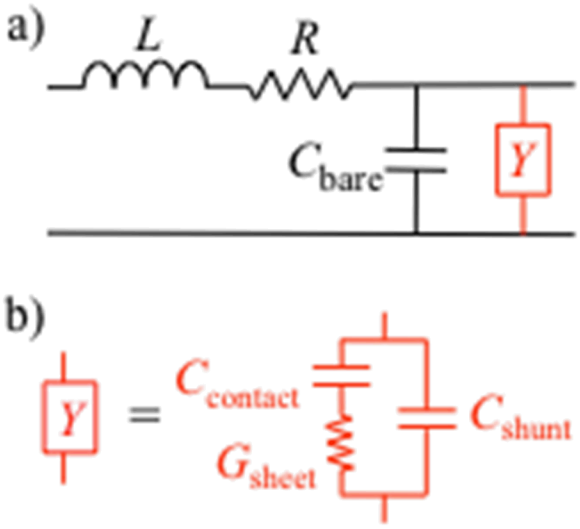

Figure 6

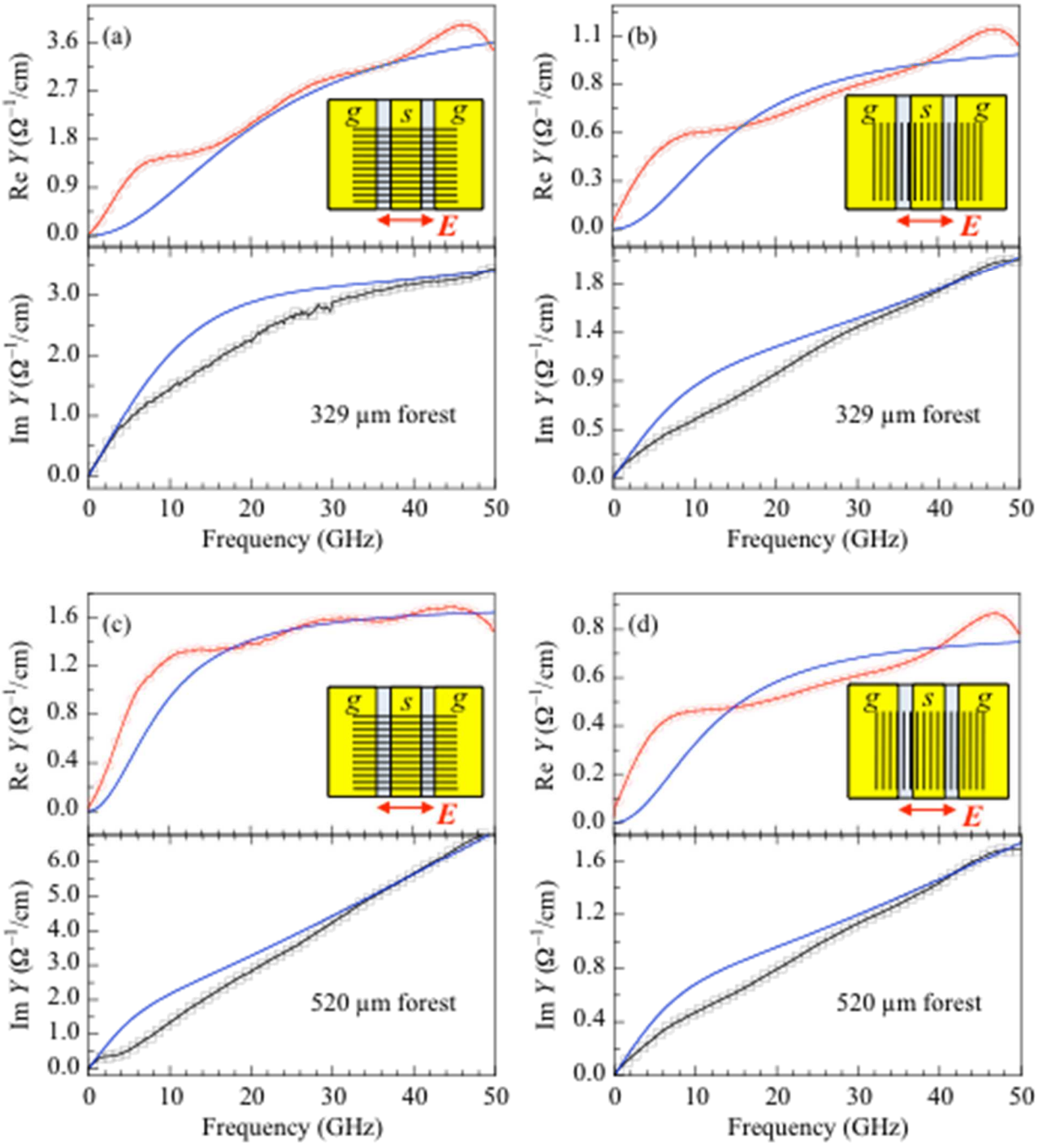
(a)
(b)
(c)
(d)
Re Y (Ω⁻¹/cm)
Im Y (Ω⁻¹/cm)
g s g
E
329 μm forest
520 μm forest
Frequency (GHz)

Figure 7

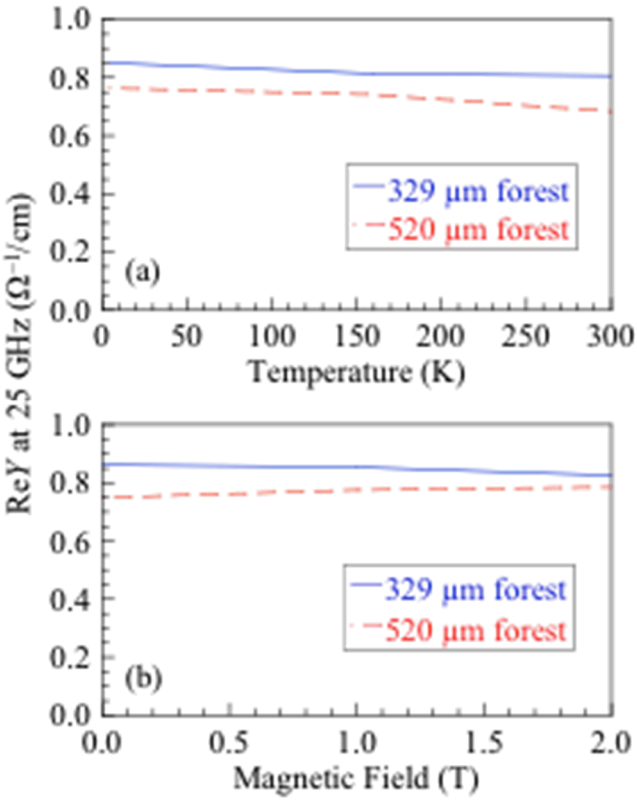
1.0
0.8
0.6
0.4
0.2
0.0
ReY at 25 GHz (Ω⁻¹/cm)
329 μm forest
520 μm forest
(a)
0
50
100
150
200
250
300
Temperature (K)
1.0
0.8
0.6
0.4
0.2
0.0
329 μm forest
520 μm forest
(b)
0.0
0.5
1.0
1.5
2.0
Magnetic Field (T)

Figure 8

[1] S. Iijima, Nature **354**, 56 (1991).
[2] M. Zhang, S. Fang, A. A. Zakhidov, S. B. Lee, A. E. Aliev, C. D. Williams, K. R. Atkinson, and R. H. Baughman, Science **309**, 1215 (2005).
[3] K. Liu, Y. Sun, L. Chen, C. Feng, X. Feng, K. Jiang, y. Zho, and S. Fan, Nano Lett. **8**, 700 (2008).
[4] Z. Kuanyshbekova, C. Huynh, S. Hawkins, D. Smagulov, S. Malayev, and A. Zakhidov, Adv. Mat. Res. **622-633,** 833 (2013).
[5] D. Jung, M. Han and G. S. Lee, J. Vac. Sci Technol. **32**, 04E105 (2014).
[6] C. Highstrete, E. A. Shaner, M. Lee, F. E. Jones, P. M. Dentinger and A. A. Talin, Appl. Phys. Lett. **89**, 173105 (2006).
[7] C. Highstrete, M. Lee, A. A. Talin and A. L. Vance, Appl. Phys. Lett. **95**, 203111 (2009).
[8] H. Xu, S. M. Anlage, L. Hu and G. Grüner, Appl. Phys. Lett. **90**, 183119 (2007).
[9] H. Xu, S. Zhang, S. M. Anlage, L. Hu and G. Grüner, Phys. Rev. B 77, 075418 (2008).
[10] J. S. Bulmer, J. Martens, L. Kurzepa, T. Gizewski, M. Egilmez, M. G. Blamire, N. Yahya and K. K. K. Koziol, Sci. Rep. **4**, 3762 (2014).
[11] J. C. Dyre and T. B. Schroeder, Rev. Mod. Phys. **72**, 873 (2000).
[12] B. L. Brown, J. S. Bykova, A. R. Howard, A. A. Zakhidov, E. A. Shaner and M. Lee, App. Phys. Lett. **105**, 263105 (2014).
[13] N. W. Ashcroft and N. D. Mermin, *Solid State Physics* (Saunders College, New York, 1976), Chap. 1.
[14] D. M. Pozar, Microwave Engineering, 4th ed. (John Wiley & Sons, Inc., Hoboken, NJ, 2012), Chap. 2.
[15] J. Zhang and T. Y. Hsiang, PIERS Online **3**, 1102 (2007).
[16] R. J. Collier, *Transmission Lines* (Cambridge University Press, New York, 2013), Chap. 4.
[17] A. Bachtold, M. S. Fuhrer, S. Plyasunov, M. Forero, E. H. Anderson, A. Zettl and P. L. McEuen, Phys Rev. Lett. **84**, 6082 (2000).
[18] O. Hilt, H. B. Brom and M. Ahlskog, Phys. Rev. B 61, R5129 (2000).
[19] E. Decrossas, M. A. El Sabbagh, V. F. Hanna and S. M. El-Ghazaly, IEEE Trans. Electromagn. Compat. **54**, 81 (2012).
[20] J. H. Chen, C. Jang, S. Xiao, M. Ishigami, M. S. Fuhrer, Nat. Nanotech. **3**, 206 2008.
[21] S. V Morozov, K. S. Novoselov, M. I. Katsnelson, F. Schedin, D. Elias, J. A. Jaszczak and A. K Geim, Phys. Rev. Lett. **100**, 016602 2008.
[22] E. H. Hwang and S. Das Sarma, Phys. Rev. B **77**, 115449 2008.
[23] S. Piscanec, M. Lazzeri, F. Mauri and A. C. Ferrari, *The European Physical Journal of Special Topics*, Vol. 148, Issue 1, September 2007.
[24] D. Jung, S. Lee, K. H. Lee, D. Burk, L. J. Overzet and G. S. Lee, Sens. Actuators A, **199**, 176 (2013).
[25] M. Barberio, M. Camarca, P. Barone, A. Bonanno, A. Oliva and F. Xu, Surf. Scie. **601**, 2814 (2007).
[26] N. Koratkar, A. Modi, E. Lass and P. Ajayan, J. Nanosci. Nanotechnol. **4(7)** 744 2004.
[27] P. L. McEuen, M. Bockrath, D. H. Cobden and J. G. Lu, Microelect. Eng. **47**, 417 (1999).
[28] L. Langer, V. Bayot, E. Grivei, J. P. Issi, J. P. Heremans, C. H. Olk, L. Stockman, C. Van Haesendonck and Y. Bruynseraede, Phys. Rev. Lett. **76**, 479 (1996).

[29] Y. Simsek, L. Ozyuzer, A. T. Seyhan, M. Tanoglu and K. Schulte, J. Mater. Sci. 42, 9689 (2007).
[30] Y. Wei, K. Jiang, X. Feng, P. Liu, L. Liu and S. Fan, Phys. Rev. B **76**, 045423 (2007).
[31] A. E. Aliev, C. Guthy, M. Zhang, S. Fang, A. A. Zakhidov, J. E. Fisher and R. H. Baughman, Carbon 45, 2880 (2007).